Journal of the American College of Cardiology
© 2000 by the American College of Cardiology
Published by Elsevier Science Inc.

Vol. 36, No. 6, 2000
ISSN 0735-1097/00/$20.00
PII S0735-1097(00)00941-4

Obstacle-Induced Transition from Ventricular Fibrillation to Tachycardia in Isolated Swine Right Ventricles

Insights into the Transition Dynamics and Implications for the Critical Mass

Miguel Valderrábano, MD, Young-Hoon Kim, MD, FACC, Masaaki Yashima, MD, Tsu-Juey Wu, MD, Hrayr S. Karagueuzian, PHD, FACC, Peng-Sheng Chen, MD, FACC

Los Angeles, California

OBJECTIVES The study was done to test the hypothesis that an artificial anatomical obstacle prevents the maintenance of ventricular fibrillation (VF) by stabilizing reentrant wavefronts (RWF) and increases the critical mass (CM) of myocardium required to sustain VF.

BACKGROUND Artificial obstacles can anchor RWF in simulated models of VF. Whether an artificial obstacle affects multiple-wavelet VF in real tissue is unclear.

METHODS The endocardial surfaces of seven isolated, perfused swine right ventricles were mapped using a plaque of 477 bipolar electrodes with 1.6-mm resolution. An 8-mm hole was punched in the tissue. The CM was reached by tissue mass reductions, at which VF converted to periodic activity (ventricular tachycardia, VT).

RESULTS After the creation of the obstacle, the VF cycle length increased from 71.6 ± 18.4 ms to 87.5 ± 13.0 ms ($p < 0.05$). The obstacle, together with the papillary muscle, facilitated the transition from VF to VT by serving as attachment sites for the RWF. When one RWF attaches to the obstacle and another attaches to the papillary muscle, it may result in stable VT with figure-eight patterns. The CM for VF in the presence of an 8-mm hole (28.7 ± 3.8 g) was higher than in the control group (swine right ventricles without holes, 24.0 ± 3.4 g, $p < 0.05$).

CONCLUSIONS An artificial anatomical obstacle induces slowing and regularization of VF, impairs the persistence of VF as judged by an increase of the CM, and can convert VF to VT by serving as an attachment site to reentrant excitation. (J Am Coll Cardiol 2000;36:2000–8) © 2000 by the American College of Cardiology

Obstacles have been used extensively to study reentry (1–7). Naturally occurring obstacles, like arteries and other anatomical inhomogeneities, can attach a drifting spiral wave and make it stationary (8,9). Similarly, artificial obstacles may convert a meandering (detached) reentrant wavefront (RWF) into a stable (attached) one in an experimental (5) and simulated (6,9) two-dimensional (2D) tissue. In simulated three-dimensional (3D) tissue a full-thickness obstacle is capable of attaching a *single* drifting scroll wave, whereas a partial-thickness obstacle produces unstable attachment (10). Whether this holds true in real 3D tissue that sustains multiple-wavelet ventricular fibrillation (VF) remains unclear. We (11) reported that persistent and stable multiple-wavelet VF may be induced in the isolated, perfused swine right ventricle (RV). Gradual reduction of the tissue mass resulted in the reduction of the number of wavelets and eventually the termination of VF or the conversion from VF to ventricular tachycardia (VT) when a critical mass (CM) (12) was reached. The papillary muscle (PM) played a key role as an attaching structure to RWF during VT (13). However, the presence of PM did not prevent the maintenance of VF. The purpose of the present study was 1) to assess the influence of a full-thickness artificial obstacle on the dynamics of multiple-wavelet VF; 2) to determine whether an artificial obstacle can convert VF to VT by stabilizing RWF; and 3) to determine the effects of an artificial obstacle on the CM for VF.

METHODS

Experimental preparation. The study protocol was approved by the Institutional Animal Care and Use Committee. The experimental model has been previously described (11). Briefly, the hearts of seven farm pigs were quickly removed and placed in oxygenated Tyrode's solution at 37°C. The right coronary artery was cannulated and perfused with Tyrode's solution. The RV was excised; VF occurred in vivo during excision, and persisted in vitro. The fibrillating RV was then placed in a tissue bath with the endocardial surface facing on a built-in electrode array on the bottom of the tissue bath with 477 bipolar electrodes, 1.6 mm apart, arranged in 20 columns and 25 rows. The

From the Division of Cardiology, Department of Medicine, Cedars-Sinai Medical Center, and UCLA School of Medicine, Los Angeles, California. This study was supported by a Korea University fellowship grant (Y.-H.K.); a Cedars-Sinai ECHO Foundation Award; an A.H.A. National Center Grant-in-Aid (9750623N and 9950464N); a TRDRP (6RT-0020); a NIH SCOR grant in sudden death (P50-HL52319); the Pauline and Harold Price Endowment (P.-S.C.); and the Ralph M. Parsons Foundation.

Manuscript received September 16, 1999; revised manuscript received May 12, 2000, accepted July 12, 2000.

Abbreviations and Acronyms

CL = cycle length
CM = critical mass
pECG = pseudoelectrocardiogram
PM = papillary muscle
RWF = reentrant wavefront
SD = standard deviation
2D = two-dimensional
VF = ventricular fibrillation
VT = ventricular tachycardia

PM was cut to improve electrode contact. Data were acquired by a computerized mapping system (Unemap, Uniservices, New Zealand) at 1,000 samples per second with 16 bits of accuracy (11). Pseudoelectrocardiograms (pECG) were recorded from two electrodes placed on the opposite edges of the tissue (Fig. 1).

An 8-mm-diameter cylindrical obstacle (hole) was then created using a skin biopsy punch (5). The specific location of the obstacle within the tissue was determined by the need to avoid major epicardial arteries, but in general the hole was created near the center of the tissue, at variable distances from the PM. Several 8-s recordings were acquired before and after the creation of the obstacle.

Progressive tissue mass reduction was achieved by cutting 0.3 g to 1.5 g from the boundary of the tissue (11). If VF continued, additional tissue was removed. A transition from VF to VT was judged to occur when a regular and largely repeated pattern of activation was present consistently. Polymorphic or transient (<30 s) VT was not considered a transition. The CM for spontaneous VF was defined as the tissue weight at which spontaneous VF converted to VT. The VF was reinduced by rapid pacing at different sites; VF was considered induced if it persisted for >5 s after pacing. After successful VF reinduction, additional tissue mass reductions were made until VF could not be induced. A minimum of four different pacing sites were used before considering VF as noninducible. At the end of the experiments, bipolar diastolic pacing thresholds were measured at a minimum of five sites in the region around the obstacle. Data were compared with baseline threshold determined at similar locations.

Control data. An additional tissue was used as control. The tissue preparation was as described, including obstacle creation, but no mass reductions were performed so that the effects of the obstacle at masses above the CM could be studied. To compare CM with and without the obstacle, we used our previous studies as a control (11). In that study, the tissue preparation and experimental procedures were exactly the same, but no obstacle was placed.

Data analysis. The methods of computerized mapping have been previously reported (14). Patterns of activation were displayed dynamically on the computer screen (15). We defined attachment of a RWF to the obstacle as a mode of activation when the tip of consecutive RWFs followed a path corresponding to the boundary of the obstacle (5). In this situation, the cross-sectional area of the obstacle was the size of the core. If attachment did not occur around the obstacle, then the size of the core was calculated by tracing the point on the RWF closest to the core. The area encircled by these points was the core size (15). The number of RWFs at a given instant of VF was defined as the number of activations separated from each other by recovered but nonactivated tissue (11). A mean VF cycle length (CL) was obtained for each channel by averaging the interactivation intervals. The VF CL of the entire tissue was calculated by averaging CLs of all channels. Standard deviation (SD) of the VF CL was used to assess the variability of VF CL recorded by each channel. Slowing and regularization of VF were defined as significant increases and decreases of VF CL and VF SD, respectively. For comparisons, data were pooled from two 8-s recordings before and after creating the obstacle.

All data are presented as mean ± SD and were compared using the Student *t* test when appropriate. Two-way repeated-measures analysis of variance (ANOVA) was used to compare VT CL before and after obstacle creation, and in and out of the surrounding rim of channels. Linear regression analysis was used to determine the relation between the core size and VT CL. A p value ≤0.05 was considered significant.

RESULTS

In one tissue, the placement of an obstacle caused immediate transition from VF to VT. In the remaining six tissues, tissue mass reductions were necessary to achieve transitions from VF to VT. Spontaneous annihilation of all electrical activity occurred at the end of the experiments, only after converting to VT (never from VF). The pacing thresholds at the end of the experiments did not differ significantly from that obtained before punching the hole (0.55 ± 0.36 mA vs. 0.47 ± 0.26 mA, p = NS).

Effects of the obstacle on VF. The characteristics of VF changed immediately after creation of the obstacle. The mean VF CL increased in all tissues. In all but one tissue, there was a decrease in the SD of VF CL (Table 1). In dynamic display, baseline VF was characterized by the presence of multiple wavelets coexisting in the tissue. The creation of an obstacle did not change significantly the number of wavelets present in the tissue at any given time (from 4.8 ± 0.7 to 4.4 ± 1.3), except in one tissue. During baseline VF, we observed RWFs attached to the PM insertion for an average of 1.5 ± 1.4 cycles (13) at a time in the span of two 8-s recordings. After creation of the obstacle, attaching to the obstacle was seen with a mean of 1.7 ± 1.5 cycles. Anchoring to either structure occurred at different times in a given tissue, but the coexistence of RWF attaching to both the PM and the obstacle simultaneously was not seen during VF.

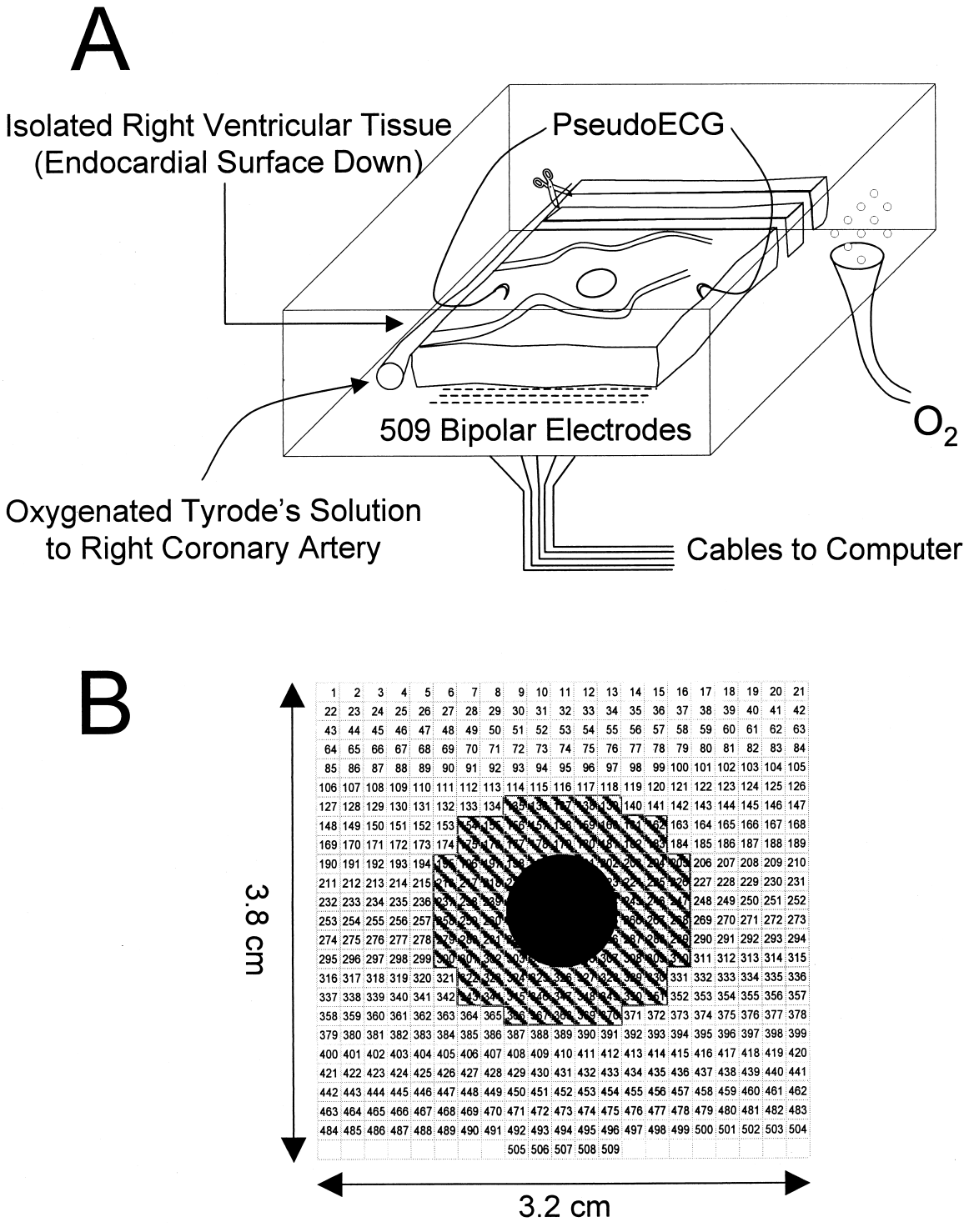

Figure 1. Recording methods. (**A**) Schematic representation of the tissue preparation. (**B**) Electrode distribution. The shaded area shows the location of electrodes used for calculations in Table 1.

Before creating the hole, the average VF CL and its SD distributed evenly. After the hole was created, an area of increased VF CL and decreased SD of VF CL was clearly detected around the obstacle. Comparison of a rim of three-channel width (Fig. 1) around the obstacle showed prominent increase and decrease, respectively, of the mean VF CL and VF SD (Table 1). Creating the obstacle resulted in significant changes in VF CL of the whole tissue and in the rim channels. Testing for interaction was also significant ($p = 0.0007$).

In the control tissue, VF persisted for 4 h and 17 min. The number of wavefronts remained stable over time (4.6 ± 1.2, 4.2 ± 1.5, 4.9 ± 1.1, and 4.2 ± 1.4, p = NS, at 1-h intervals).

Table 1. Characteristics of Ventricular Fibrillation and Ventricular Tachycardia

	During VF				During VT		
	Whole Tissue		Rim channels				
Tissue No.	CL Preobstacle	CL Postobstacle	CL Preobstacle	CL Postobstacle	Morphology (no.)‡	Core Sizes§ (cm^2)	Mean VT CL‖
1	74.3 ± 14.9	89.8 ± 14.8*	73.5 ± 15.9	111.8 ± 13.8†	SRWF (6)	0.9	233.9 ± 12.2
2	61.7 ± 17.9	78.3 ± 12.9*	63.3 ± 18.7	107.9 ± 7.4†	F8 (3)	0.42, 0.5	115.1 ± 6.2
3	76.2 ± 21.1	83.4 ± 15.9*	75.3 ± 19.5	108.2 ± 8.9†	SRWF (5)	0.83	229.6 ± 13.5
4	69.7 ± 19.0	79.2 ± 12.9*	68.7 ± 18.6	99.5 ± 7.5†	F8 (4)	0.51, 0.5	102.1 ± 5.8
5	78.9 ± 22.2	112.7 ± 4.9†	79.7 ± 21.8	112.6 ± 5.0†	F8 (3)	0.38, 0.5	112.7 ± 5.0
6	68.6 ± 18.2	82.4 ± 15.1*	70.1 ± 19.5	100.4 ± 11.6†	F8 (4)	0.34, 0.5	101.2 ± 7.9
7	72.0 ± 16.2	86.5 ± 14.1*	71.8 ± 16.7	98.7 ± 8.7†	F8 (3)	0.54, 0.5	119.9 ± 1.8
All data	71.6 ± 18.4	87.5 ± 13#	71.7 ± 18.7	105.9 ± 9.0**			

* = $p < 0.05$; † = $p < 0.001$ compared to Preobstacle values; ‡not included: one episode of incomplete F8 (tissue 6), two episodes of breakthrough activation (tissue 5), and one episode of incomplete F8 (tissue 7); §in SRWF, core includes the hole (always 0.5 cm^2) and the adjacent papillary muscle. In F8 episodes, the two figures indicate the area of the papillary muscle and the hole; respectively; ‖Several CLs occurred on a given tissue; #$p = 0.0256$ by two-way, repeated measures ANOVA; **$p < 0.0001$ by two-way, repeated measures ANOVA.

CL = cycle length in ms; F8 = figure-eight; SRWF = single reentrant wavefront.

The obstacle and the transition from VF to VT. Tissue mass reductions caused a net decrease in the number of wavefronts in the mapped region (from 4.4 ± 1.3 to 3.3 ± 0.8, $p < 0.05$) before the conversion to VT. We successfully mapped a total of 9/32 spontaneous transitions. All nine mapped transitions showed attachment of a RWF to the obstacle. In six of them, the transition occurred after a single RWF attached to an area comprised both of the obstacle and the root of the PM. Figure 2 shows an example. Starting in VF (panels A and B), multiple wavelets are seen that completely excite the surroundings of the obstacle (wavelets marked with an asterisk and with a diamond in panels J and M). In panel C, a new RWF (marked with a circle in panels K and M), arising as endocardial breakthrough activation, arrives at the obstacle. The activation proceeds clockwise around the obstacle. However, as shown in panels E and F, it does not complete a full rotation around the obstacle. Instead, after completion of roughly two-thirds of a circle, there is an area of block and the activation turns around it and eventually completes a full reentrant excitation. In this tissue, the obstacle was placed very close to the PM (panels K and L). The PM facilitated the development of block (panel E). This pattern was maintained in subsequent rotations without wavefront detachment. The core of the reentry was formed by the summation of two structures: the artificial obstacle and the root of the PM, which were in contact with each other. There was remarkable conduction slowing around the PM (panel K).

In the remaining three transitions mapped, there was a coexistence of two RWFs. Figure 3 illustrates an example. During VF (panel A), multiple RWFs coexist, with an almost complete excitation of the obstacle's boundaries. Later on (panel B), a RWF approaches the obstacle, but before arriving at its boundaries it finds an area of conduction block and splits into two daughter wavelets. One (plus sign, yellow arrows) arrives at the right side of the obstacle and turns around it (panels C through E), while the other (asterisk, white arrows) proceeds down and turns around, arriving at the left side of the obstacle almost simultaneously with the first wavefront (panel F). A figure-eight pattern is formed. These two reentrant circuits have identical CLs. In this tissue, the location of the obstacle relative to the PM insertion allowed the presence of a narrow isthmus between them (panels I and J). The obstacle served as the core for one RWF, whereas the PM served as the core for the other. This was stable over time, and no wavefront detachment to either structure was seen. Both circuits shared a common isthmus, where conduction time was slowest.

Whereas creation of an obstacle resulted in immediate and predictable VF slowing and regularization, obstacle-induced transitions to VT were unpredictable. The RWF attaching to the obstacle mediated stabilization of reentry and transition from VF to VT. Figures 2 and 3 showed an initial phase of VF where multiple RWFs activated different portions of the tissue, including the PM. Immediately before transition to VT, multiple wavelets arrived at the obstacle almost simultaneously (Figs. 2B and 3A). As a result, the tissue surrounding the obstacle became activated within a short period of time, causing almost synchronous recovery of excitability. By the time a new RWF arrived at the obstacle (Figs. 2C and 3B), all its boundaries were excitable. The RWF could therefore proceed along the obstacle's borders, leading to attachment. There was a critical delay between the last excitation of the obstacle's boundaries by any RWF during VF and the arrival of the RWF that attached and initiated VT. This coupling time was calculated to be 148 ± 41 ms (range 100 to 235 ms).

Characteristics of VT. We mapped 32 VT episodes (Table 1), including 9 episodes immediately after transition and 23 episodes of sustained VT. There were primarily two patterns of activation: 1) a single RWF rotating around the obstacle and the PM (n = 11); 2) a figure-eight where one RWF rotated around the obstacle and the other around the PM (n = 17). In addition, one episode showed an incomplete

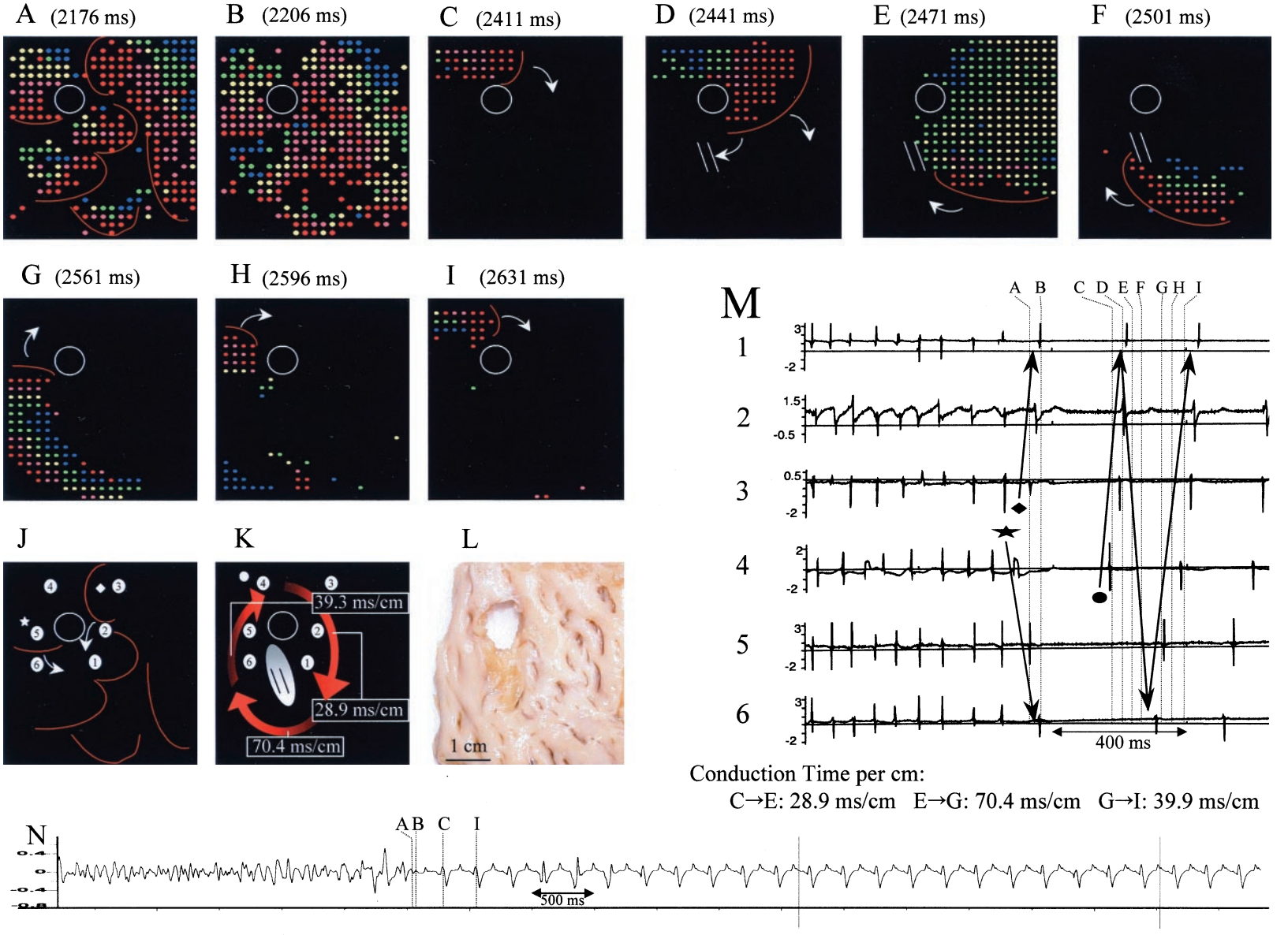

Figure 2. Transition from VF to VT by attaching a RWF to the obstacle and PM insertion. The numbers above the snapshots indicate time after the beginning of data acquisition. **Panels A–I** show activation during VF (**panels A** and **B**) and the transition to VT (**panels C–I**). **Panels J** and **K** show a schematic representation: wavefronts marked as an asterisk and a diamond activate the obstacle's boundaries. Later on, a wavefront marked with a circle attached to it. Conduction time was longest when turning around the PM. **Panel L** shows the mapped tissue, with PM next to the obstacle. Note that activation maps are mirror-images of the mapped endocardial side. Therefore, **panel J** was shown in its mirror-image to match with the activation maps. **Panel M** shows local electrograms of selected channels (marked with numbers in **panels J** and **K**). **Panel N** shows the pECG, with the transition from VF to VT.

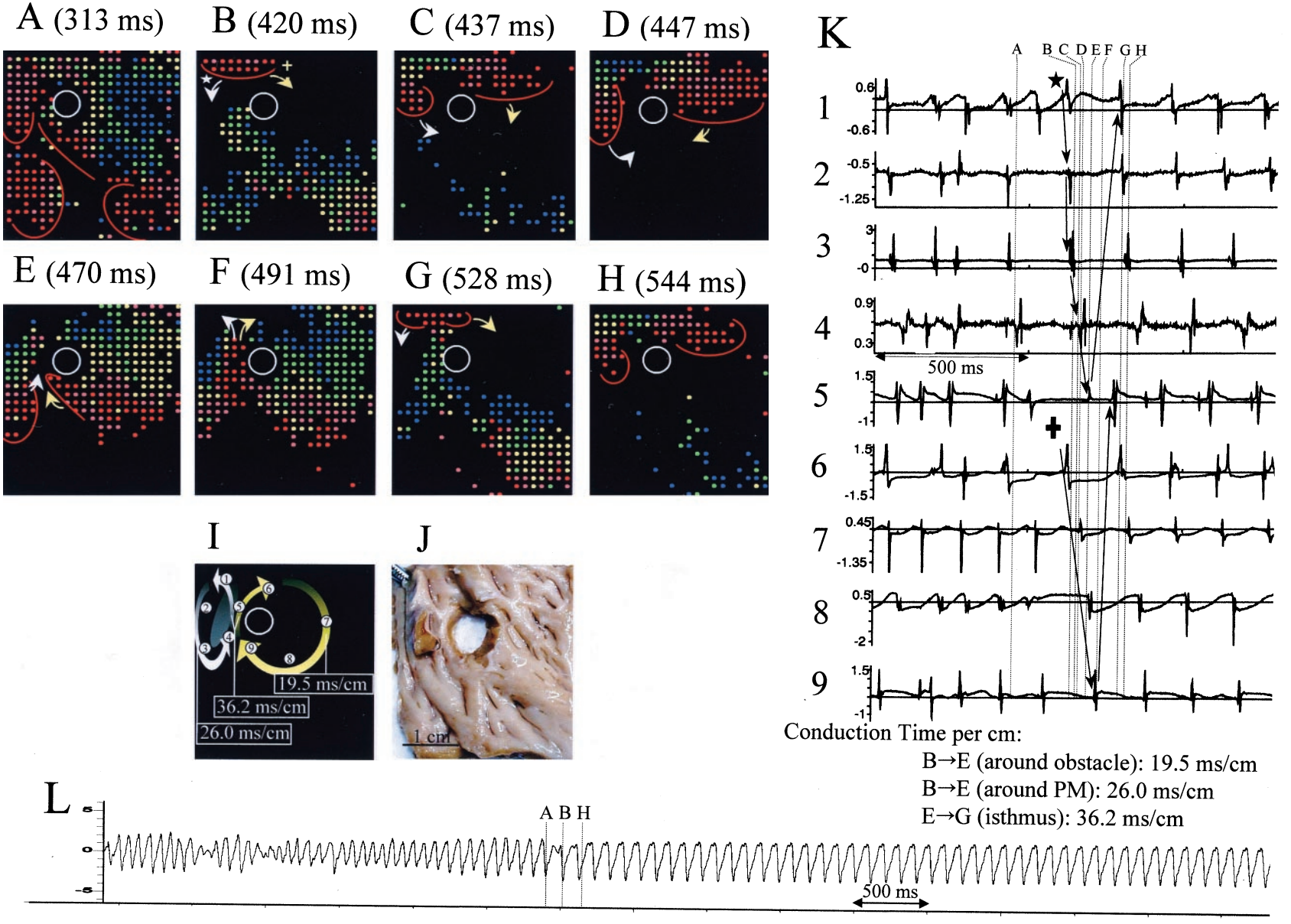

Figure 3. Transition from VF to VT by formation of a figure-eight. **Panel A**, activation during VF. **Panels B–H**, transition to VT by formation of a figure-eight. See text for details. **Panel I**, schematic representation, with conduction velocities in different portions of the reentrant circuit (the slowest in the isthmus). **Panel J** shows the tissue with the PM next to the obstacle and an isthmus in between the two. **Panel K**, shows local electrograms of channels marked in **panel I**. Wavefronts marked with asterisk and plus sign in panel B are the initiators of VT. Channel 5, located at the isthmus, is shared by both circuits and shows double potentials. **Panel L**, pECG of the transition from VF to VT.

figure-eight activation rotating around the obstacle and the PM, which failed to complete a full circle. In another episode, two stable RWFs rotated clockwise with identical CLs. Both the obstacle and the PM were located in-between these rotating RWFs and therefore did not appear to play a role as substrates for attachment. Finally, in two other episodes, a repetitive pattern of breakthrough activation arising in different parts of the tissue was seen, with no obvious reentrant circuits.

The VTs associated with a single RWF had a CL of 232.5 ± 18.5 ms, whereas those with two RWFs (either figure-eight or two separated RWFs) had a CL of 108.6 ± 9.3 ms ($p < 0.001$). In the VT episodes caused by a single RWF, the core was comprised of both the obstacle and the PM insertion, and its size was estimated by the summation of both areas. In the figure-eight episodes, the core size used for calculations was the mean of the obstacle size and the size of the PM (as each structure was attaching one RWF). Figure 4 shows the method of core size calculation in two examples (single RWF and figure-eight) of stable VT. Because the VT morphology was largely determined by the location of the obstacle relative to the PM, it did not change in a given tissue after several VF–VT transitions. Ventricular tachycardia CL did vary slightly (see Table 1). There was a positive linear correlation (correlation coefficient, 0.96, $p < 0.001$) between core sizes and CLs, following the equation

$$y(\text{CL in ms}) = -28.0 + 294.1x(\text{core size in cm}^2).$$

Areas of increased curvature, such as turning around PM (see panel K in Fig. 2, or panel P in Fig. 4, or those in a narrow isthmus of a figure-eight (panel I in Fig. 3), had the longest conduction times, implying slow conduction through a narrow isthmus (16). Figure 4 shows an example of a figure-eight with a wide isthmus in which conduction time was unaltered.

The critical mass. With the obstacle, the calculated CM for spontaneous VF was 28.7 ± 3.8 g, or 21.3 ± 1.6% of the total heart weight. Without the obstacle, the value was 24.0 ± 3.4 g, or 16.7 ± 3.5% of the total heart weight (11) ($p < 0.05$). Similarly, the CM for inducible VF with the obstacle was significantly higher (27.3 ± 4.6 g, or 20.2 ± 2.2% of the total heart weight vs. 19.9 ± 4.2 g or 13.7 ± 3.6% of the total heart weight), with $p < 0.01$. We found no differences in CM in those tissues with figure-eight VF-to-VT transitions compared to those with single RWF.

DISCUSSION

There are several major findings of the present study: 1) in multiple-wavelet VF, the RWFs may attach to an artificial obstacle, resulting in VF slowing and regularization; 2) tissue mass reduction results in stable attachment of RWF to the artificial obstacle and PM, leading to the transition from VF to VT; and 3) an obstacle increases the CM required to sustain VF.

The obstacle as a substrate for reentry stabilization during VF. To our knowledge, this is the first experimental description of the reentry-stabilizing properties of an artificial obstacle in the setting of multiple-wavelet VF in a real 3D tissue. The obstacle induced transient RWF attachment during VF (1.7 ± 1.5 cycles), leading to less frequent and more regular activations around the hole. These findings are compatible with 2D simulation studies (6) that suggested stable spiral wave attachment was due to the stabilizing effect of CL prolongation in the presence of a sufficiently large obstacle. In simulated 3D excitable media with a single drifting scroll wave, Vinson et al. (10) showed that a full-thickness obstacle would behave similar to a 2D obstacle, inducing scroll wave attachment. However, we only detected transient attaching to the obstacle during VF, as invasion by other wavelets prevented stabilization. Stable attachment occurred only when the tissue mass (hence the number of wavelets) (11) was reduced.

We found that the VF-to-VT transition occurred only when a wavefront arrived at the obstacle after its boundary had recovered from refractoriness. The need for the coexistence of simultaneously recovered boundary tissue explains the unpredictability (probability factor) of the time of transition after a hole is punched.

Interaction between the PM and the acquired anatomical obstacle. The stump of the PM increases the anatomical heterogeneity in the endocardial portion of the RV. In simulated 3D tissue (10), such a partial-thickness obstacle can only temporarily attach a *single* scroll wave. Afterwards the portion of the filament not attached can pull the scroll wave away from its temporary attachment. The number of rotations that a scroll wave remains attached to the obstacle depends on the thickness of the obstacle relative to the thickness of the tissue. These findings may explain the relative lack of efficacy of PM in attaching reentry during baseline VF. By creating a transmural full-thickness obstacle, we were able to immediately increase the VF CL by creating a more effective attachment for the RWF. In other words, the full-thickness artificial obstacle provides filament stabilization at masses when attaching to just the PM alone would be unstable. Furthermore, smooth contours and uniform curvature of the hole may impair vortex shedding (17) and limit wavelength variations (18), favoring RWF attachment and possibly mediating this antifibrillatory effect. These phenomena might explain the increased CM for VF after punching a hole.

The anatomical and functional relationship between the PM and the obstacle was crucial in determining the type of transition to VT. The presence of an isthmus between them—more likely if widely separated, but possible even if close to each other as in Figure 3—allowed for figure-eight patterns. This relationship, however, did not impact the effect of the obstacle in VF slowing or CM.

Study limitations. Although we studied the effects of an obstacle in a 3D tissue, we mapped exclusively the endocardial side. Therefore, we were not able to confirm the

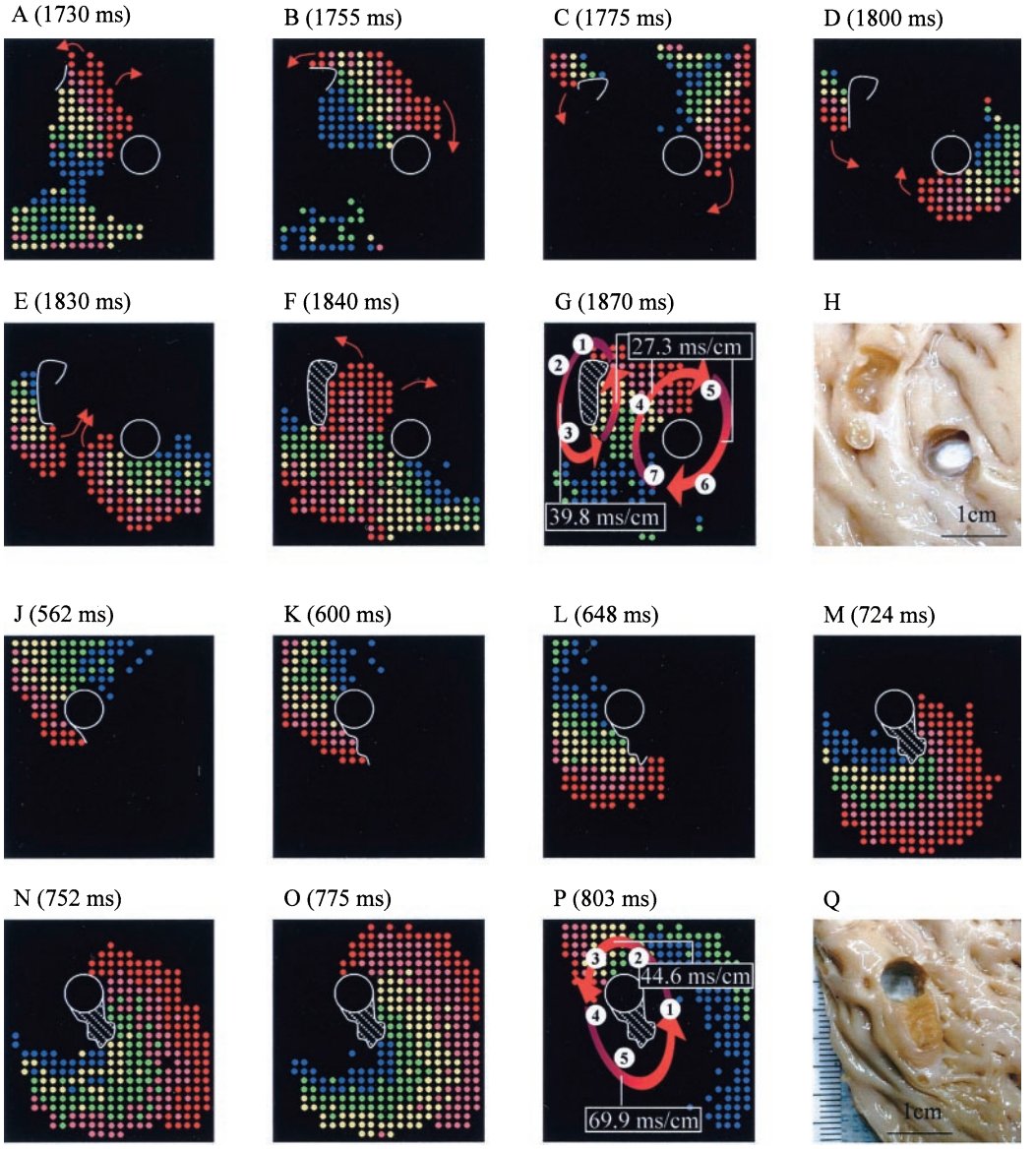

Figure 4. Core size calculation in figure-eight and single RWF VT. **Panels A–G**, example of a figure-eight pattern, where the core of the right-most reentrant circuit is formed by the obstacle (8-mm diameter). In the left, the RWF rotates counterclockwise. By consecutively joining the red dots, the core of this RWF can be delineated. In **panel G**, numbers show the location of the channels whose local electrograms are selected for demonstration in **panel I**. Also shown are the conduction velocities that are uniform around the obstacle but slowest in regions of increased curvature around the PM. **Panels J–R**, on a different tissue, the same method applied to a case of single RWF rotating clockwise. The core of this rotation is formed in part by the hole. However, when the activation proceeds inferior to the hole, it goes downward, where the PM was located (**panels K, L** and **M**). In **panel M**, the activation again contacts the hole's boundaries. By joining the red dots, the area surrounded by the activation next to the hole can be identified (the PM insertion) and its area calculated. The summation of this area and the area of the hole is considered the core size. **Panel P** shows selected channels whose electrograms are shown in **panel R**, and conduction time longer around the PM. **Panels H** and **Q** are mirror-images of the respective tissues.

presence of the scroll waves or study the dynamics of the filaments. We did not control the location of the obstacle relative to the PM because of the need to avoid damaging the coronary arteries. This concern has limited our abilities to evaluate fully the interaction between the hole and the PM. Another limitation is that we cannot fully rule out the presence of tissue injury after punching a hole. However, because the pacing threshold around the hole remained normal, and that wavefront attachment occurred primarily around the hole, we believe the tissue remained viable throughout the study. Finally, we used data from our previously reported work (11) as controls, but the identical experimental conditions allowed valid statistical comparison.

Implications. We provide evidence supporting the antifibrillatory properties of a full-thickness, cylindrical obstacle. Similar physiologic effects could be expected with obstacles that do not necessarily break the tissue integrity, and that could be created by radiofrequency energy or by other surgical techniques. Whether this proves clinically feasible remains to be investigated.

Acknowledgments

The authors wish to thank Avile McCullen, Nina Wang, and Meiling Yuan for technical help, and Elaine Lebowitz for secretarial assistance.

Reprint requests and correspondence: Dr. Peng-Sheng Chen, Room 5342, CSMC, 8700 Beverly Blvd., Los Angeles, California 90048-1865. E-mail: chenp@csmc.edu.

REFERENCES

1. Mines GR. On circulating excitation in heart muscles and their possible relation to tachycardia and fibrillation. Trans R Soc Can 1914;4:43–53.
2. Rosenblueth A, Ramos JG. Studies of flutter and fibrillation. II. The influence of artificial obstacles on experimental auricular flutter. Am Heart J 1947;33:677–84.
3. Brugada J, Boersma L, Kirchhof CJ, Heynen VV, Allessie MA. Reentrant excitation around a fixed obstacle in uniform anisotropic ventricular myocardium. Circulation 1991;84:1296–306.
4. Bernstein RC, Frame LH. Ventricular reentry around a fixed barrier. Resetting with advancement in an in vitro model. Circulation 1990; 81:267–80.
5. Ikeda T, Yashima M, Uchida T, et al. Attachment of meandering reentrant wave fronts to anatomic obstacles in the atrium. Role of the obstacle size. Circ Res 1997;81:753–64.
6. Xie F, Qu F, Garfinkel A. Dynamics of reentry around a circular obstacle in cardiac tissue. Phys Rev E 1998;58:6355–8.
7. Girouard SD, Pastore JM, Laurita KR, Gregory KW, Rosenbaum DS. Optical mapping in a new guinea pig model of ventricular tachycardia reveals mechanisms for multiple wavelengths in a single reentrant circuit. Circulation 1996;93:603–13.
8. Davidenko JM, Pertsov AM, Salomonsz R, Baxter W, Jalife J. Stationary and drifting spiral waves of excitation in isolated cardiac tissue. Nature 1992;355:349–51.
9. Pertsov AM, Davidenko JM, Salomonsz R, Baxter WT, Jalife J. Spiral waves of excitation underlie reentrant activity in isolated cardiac muscle. Circ Res 1993;72:631–50.
10. Vinson M, Pertsov A, Jalife J. Anchoring of vortex filaments in 3D excitable media. Physica D 1993;72:119–34.
11. Kim YH, Garfinkel A, Ikeda T, et al. Spatiotemporal complexity of ventricular fibrillation revealed by tissue mass reduction in isolated swine right ventricle. Further evidence for the quasiperiodic route to chaos hypothesis. J Clin Invest 1997;100:2486–500.
12. Garrey WE. The nature of fibrillatory contraction of the heart—its relation to tissue mass and form. Am J Physiol 1914;33:397–414.
13. Kim Y-H, Xie F, Yashima M, et al. Role of papillary muscle in the generation and maintenance of reentry during ventricular tachycardia and fibrillation in isolated swine right ventricle. Circulation 1999;100: 1450–9.
14. Bonometti C, Hwang C, Hough D, et al. Interaction between strong electrical stimulation and reentrant wavefronts in canine ventricular fibrillation. Circ Res 1995;75:407–16.
15. Lee JJ, Kamjoo K, Hough D, et al. Reentrant wave fronts in Wiggers' stage II ventricular fibrillation: characteristics, and mechanisms of termination and spontaneous regeneration. Circ Res 1996;78:660–75.
16. Cabo C, Pertsov AM, Baxter WT, Davidenko JM, Gray RA, Jalife J. Wavefront curvature as a cause of slow conduction and block in isolated cardiac muscle. Circ Res 1994;75:1014–28.
17. Cabo C, Pertsov AM, Davidenko JM, Baxter WT, Gray RA, Jalife J. Vortex shedding as a precursor of turbulent electrical activity in cardiac muscle. Biophys J 1996;70:1105–11.
18. Dillon SM, Allessie MA, Ursell PC, Wit AL. Influences of anisotropic tissue structure on reentrant circuits in the epicardial border zone of subacute canine infarcts. Circ Res 1988;63:182–206.